Oxygen-Doped Carbon Supports Modulate the Hydrogenation Activity of Palladium Nanoparticles Through Electronic Metal-Support Interactions

Radhika G. Rao,[1,2] Raoul Blume,[3] Mark T. Greiner,[3] Pei Liu,[4] Thomas W. Hansen,[4] Kathleen S. Dreyer,[5] David D. Hibbitts,[5] and Jean-Philippe Tessonnier[1,2,]*

[1] Department of Chemical and Biological Engineering, Iowa State University, Ames, Iowa 50011, United States

[2] Center for Biorenewable Chemicals (CBiRC), Ames, Iowa 50011, United States

[3] Max Planck Institute for Chemical Energy Conversion, Heterogeneous Reactions Group, 45470 Mülheim an der Ruhr, Germany

[4] National Centre for Nano Fabrication and Characterization, DTU Nanolab, Technical University of Denmark, Lyngby 2800, Denmark

[5] Department of Chemical Engineering, University of Florida, Gainesville, Florida 32611, United States

KEYWORDS: Electronic Metal-Support Interactions, Oxygen Doping, Carbon Supports, Selective Hydrogenation, Work Function, Charge Transfer.

ABSTRACT

In heterogeneous catalysis, synergies between the metal active phase and oxide support can enhance the catalytic activity through electronic metal-support interactions (EMSI). Such effects are unexpected for conventional carbon supports and carbon is often viewed as an inert scaffold in catalysis. Here, we demonstrate that carbons do present EMSI that alter the intrinsic rate of palladium atoms near the interface by 200-fold compared to atoms at the apex of 5 nm particles. We also show that oxygen-containing functional groups, which are ubiquitous on carbon surfaces, are responsible for these EMSI. Controlling the scaffold's surface chemistry allowed us to tune its work function from 5.1 to 4.7 eV, the intensity of the charge redistribution at the metal-carbon interface, and the catalytic activity of the corresponding metal atoms. The proposed platform can be applied to fundamentally understand EMSI effects for reactions and carbonaceous supports beyond those studied in the present work.

ABSTRACT GRAPHIC

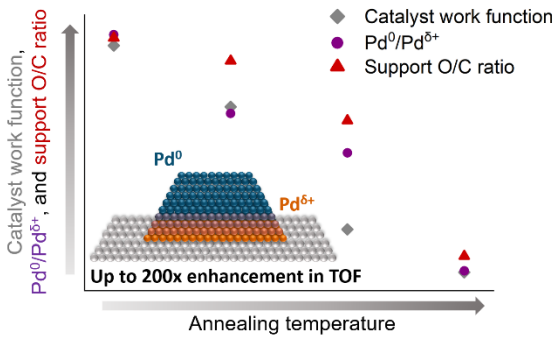

1. INTRODUCTION

The catalytic activity of supported metal nanoparticles can be significantly enhanced by tailoring the support properties, and thereby the electronic metal-support interactions (EMSI).[1-3] This enhancement in performance is typically ascribed to the flow of electrons at the interface that occurs until the Fermi levels of metal and support align, in analogy to the Mott-Schottky effect for metal-semiconductor heterojunctions.[4-8] As a result of these interactions, metal atoms may gain or lose electron density depending on the work function of the support, leading to differences in their catalytic performance.

EMSI effects are well-documented for oxide-supported catalysts.[1, 3, 7, 9] Significant changes in catalytic performance with support structure were also observed for carbon-supported metal nanoparticles.[10-14] However, the mechanisms by which topological defects and heteroatom-containing functional groups alter the catalytic activity of the supported metal atoms are still debated.[14-16] Several studies proposed that polar functional groups alter the hydrophilic-hydrophobic character of the surface, thereby influencing the reactants' adsorption mode and, as a result, the rate and selectivity of the reaction.[17-19] For the hydrogenation of cinnamaldehyde, an α,β-unsaturated model compound,[20] this interpretation is supported by infrared spectra, which revealed a strong correlation between cinnamaldehyde's adsorption mode, the support's surface polarity, and the C=C/C=O selectivity of the hydrogenation reaction.[17] However, advanced characterizations and theoretical calculations that support this causality are still missing. Therefore, it cannot be excluded that the observed switch in cinnamaldehyde's adsorption mode is driven by the change in the electronic structure of the metal active phase rather than the change in surface polarity.

Alternatively, several groups have proposed that the observed differences in catalytic activity are due electronic phenomena similar to ligand effects.[21-24] The oxygen-containing functional groups, which decorate the structural defects of carbon surfaces, could bind to the metal nanoparticles and alter the active phase's electronic structure through charge transfer.[21] In the ligand field theory, electronic density can either flow from the ligand to the metal or from the metal to the ligand depending on the position of its molecular orbitals, hence the nature of the ligand. This interpretation is consistent with the shifts in binding energy observed by X-ray photoelectron spectroscopy (XPS) for Pd and Pt nanoparticles supported on functionalized carbons.[24, 25] However, for the ligand field theory to apply, the orbitals of the transition metal atoms and ligands must overlap, implying that each metal atom must be within metal-ligand bonding distance of at least one functional group, which becomes increasingly unlikely when decreasing the surface O/C ratio. Even in the case where 25% of the surface would be covered with oxygen-containing functional groups, only about 3% of the Pd atoms in a 5 nm nanoparticle would be altered through ligand effects.[26] These effects are relevant for single-atom catalysts but extremely unlikely for conventional supported metal catalysts.

Structure-property relationships that would link carbon atom hybridization, topology, nature/concentration of surface oxygen-containing functional groups with the metal sites' electronic structure and catalytic activity are still lacking.[27] In order to close this gap and gain fundamental knowledge on strong metal-support interactions triggered by oxygen doping, here, we study the catalytic activity of palladium nanoparticles decorating carbon nanotubes (CNTs) as model carbons. By tuning the CNTs' surface chemistry and metal particle size, we show that oxygen-containing functional groups, which are ubiquitous on carbon materials, significantly alter the work function of these supports. Ultraviolet photoelectron spectroscopy (UPS) and *in situ* near-

ambient pressure X-ray photoelectron spectroscopy (NAP-XPS) are combined to unequivocally correlate oxygen concentration at the carbon surface with the work function of the support and interfacial charge transfer at the palladium-carbon boundary. The synchrotron radiation used for the NAP-XPS experiments also offers the beam intensity and energy resolution needed to study Pd/C *in situ*, in the presence of a gas atmosphere, and dismiss contributions from sub-surface oxides and hydrides to the electron-depleted $Pd^{\delta+}$ phase observed at the metal-carbon interface. The correlations between $Pd^{\delta+}$ and catalytic activity are further investigated for the liquid-phase hydrogenation of cinnamaldehyde. Combining experiments with DFT calculations, we demonstrate that EMSI induced by the carbon support alter the binding energies of the involved species and their reaction pathways. These EMSI effects are significant as they increase the intrinsic rate of Pd atoms by up to two orders of magnitude and enhance the selectivity of the catalyst.

2. EXPERIMENTAL

2.1 Catalyst Synthesis. Commercial stacked cup carbon nanotube (CNT) supports were purchased from Pyrograf Products Inc. (Ohio, USA). The CNTs were synthesized by chemical vapor deposition (CVD) and annealed at 700 °C post synthesis to give the pyrolytically stripped (PS grade) supports. This annealing process removes the polyaromatic hydrocarbons from the fiber surface without altering the morphology and textural properties of the nanotubes.[28] Prior to use, the obtained supports were treated with trace metal grade concentrated nitric acid (65% HNO_3, Fisher scientific) at 100 °C for 4 h in order to remove any impurities and to functionalize the carbon surface. The nitric acid to CNT ratio was set to 500 ml for 10 g of carbon for consistency with previous works.[26, 28, 29] Following this treatment, the oxidized CNTs were rinsed with 5 L of

deionized water (18 MΩ, Millipore) and dried overnight at 110 °C. All CNTs used in the present study were oxidized using the aforementioned treatment. Therefore, they will be referred to as CNTs from here on for conciseness.

Palladium was deposited onto the CNTs by incipient wetness impregnation. Palladium nitrate dihydrate (~40% Pd, Sigma-Aldrich) was chosen as the metal precursor due to its ease of decomposition and absence of impurities in the catalyst post synthesis. 187.5 mg of the palladium precursor was dissolved in 12.6 ml deionized water adjusted to pH 4.0 using nitric acid. The precursor solution was added dropwise to 1.5 g of oxidized supports and the mixture was then sonicated for 5 min in order for the solution to homogeneously wet the carbon surface. The impregnated supports were then dried at room temperature for 8 h, at 65 °C overnight, and at 80 °C for an additional 8 h. The impregnated samples were subsequently transferred to a quartz reactor placed in the center of a tube furnace for calcination and reduction. The dried samples were first calcined in flowing synthetic air (200 ml min^{-1}; Airgas) at 250 °C for 2 h using a 2 °C min^{-1} ramp to decompose the metal precursor. After returning to room temperature, the gas atmosphere was switched to nitrogen (200 ml min^{-1}; Airgas) for 30 minutes and then to hydrogen (200 ml min^{-1}; Airgas) and the samples were reduced at 400 °C for 2 h using a 2 °C min^{-1} ramp. Post reduction, the reactor was kept at 400 °C, flushed with nitrogen for 30 min, and the samples were further annealed under nitrogen at 400, 550, 700, or 850 °C using a 10 °C/min ramp and a dwell time of 30 min.

2.2 Catalytic investigations. The catalysts in this study were tested for the ambient pressure liquid phase hydrogenation of cinnamaldehyde. Reactions were performed in a 3-neck round bottom flask connected to a condenser maintained at 4 °C. Firstly, 100 mg of the catalyst was added to the batch reactor with 40 ml dioxane (99.8% purity, Sigma-Aldrich) and 365 mg decane

(internal standard; ≥ 99% purity, Sigma-Aldrich) along with a stir bar. The reactor was placed in an oil bath at room temperature and the solution was stirred at 500 rpm. The system was then purged with nitrogen at 20 ml min^{-1} for 20 min using a Bronkhorst mass flow controller and a fine frit (10 – 20 μm porosity) to remove any air. Following this, the gas flow was switched to hydrogen and the temperature of the oil bath was ramped to 80 °C using an IKA-RCT magnetic stir plate equipped with a PT1000 thermocouple. After 30 minutes at 80 °C, 5 g of cinnamaldehyde dissolved in 10 ml of dioxane was added to the reactor with a syringe using the third neck of the flask fitted with a rubber septum. The addition of cinnamaldehyde marked the starting time of the reaction and 200 μl of samples were then withdrawn every 15 minutes. The reaction samples were collected in pre-cooled glass vials and refrigerated to immediately quench the reaction and prevent the evaporation of the solvent. All catalytic tests were performed in triplicates.

Reactant and products were analyzed using an Agilent 7890 A gas chromatograph (GC) with an HP-5 column (30 m X 320 μm X 0.25 μm) and a flame ionization detector (FID). Prior to the analysis, samples were diluted 15 times with dioxane, filtered using 0.22 μm nylon filters, and 1 μl of this diluted sample was injected in the GC. A split ratio of 20:1 at 20 ml min^{-1}, inlet heater temperature of 300 °C, total flow of 24 ml min^{-1}, septum purge flow of 3 ml min^{-1}, and column flow of 1 ml min^{-1} was used. The initial temperature of the oven was maintained at 40 °C for 1 min and then increased to 180 °C with a ramp rate of 10 °C min^{-1}. The temperature of the FID heater was maintained at 300 °C.

2.3 Elemental analysis. The actual palladium content of each catalyst was measured using inductively coupled plasma optical emission spectroscopy (ICP-OES) (Perkin Elmer Optima 8000) and used to normalize the reaction rates. Prior to the analysis, the carbon supports of each sample were burned off by heating 30 mg of catalyst in air at 1000 °C for 6 h. The remnant

materials were soaked overnight in 5 ml aqua regia to dissolve the palladium metal. The solution was then diluted with 45 ml deionized water and analyzed. Each catalyst was analyzed in triplicates.

2.4 X-ray diffraction (XRD). XRD analysis was conducted to estimate the Pd crystallite size and characterize any phase change with increasing annealing temperature. A Siemens D-500 instrument with a copper X-ray tube, diffraction beam monochromator, a scintillation detector, a gold holder, and a medium resolution slit was used for the analysis. Two-theta values from 15 to 75 ° were scanned with a step size of 0.05 ° and a dwell time of 3 s per step. The data analysis and crystallite size estimation were conducted using the Jade software and the Scherrer equation.

2.5 Hydrogen chemisorption. Surface adsorption properties and palladium particle size were probed by hydrogen chemisorption using a static volumetric system attached to a Micromeritics ASAP 2020C instrument. 70 to 80 mg of catalyst was packed in a U-shaped chemisorption tube using quartz wool and re-reduced in situ under hydrogen at 350 °C to remove any palladium surface oxides. The tube was then evacuated, cooled down, and hydrogen was progressively reintroduced to record the adsorption isotherm under isothermal conditions (35 °C). The total amount of adsorbed hydrogen (H_T) was calculated from this first isotherm. Following this step, a vacuum was applied to remove the weakly bound hydrogen and a second adsorption isotherm was conducted to determine the reversibly bound hydrogen (H_R).

2.6 Aberration-corrected transmission electron microscopy (ac-TEM). Catalyst samples were analyzed using ac-TEM to elucidate their morphology. The samples were dispersed in ethanol on a holey carbon coated TEM grid and analyzed at 300 kV using a FEI Titan 80 – 300 equipped with a Gatan OneView CMOS camera. Aberration-corrected scanning transmission electron microscopy images were also acquired using a high-angle annular dark field detector (ac-

STEM-HAADF) to calculate average particle sizes and particle size distributions. Approximately 300 particles from multiple images were measured to ensure that the results are statistically representative.

2.7 *ex situ* X-ray photoelectron spectroscopy (XPS). X-ray photoelectron spectroscopy (XPS) studies were performed using a PHI ESCA 5500 instrument. The samples were irradiated with 225 W monochromated Al Kα X-rays and the pass energy was set at 188 eV for survey scans, 47 eV for high resolution scans, and 59 eV for valence band scans.

2.8 *in situ* near ambient pressure X-ray photoelectron spectroscopy studies (NAP-XPS). The *in situ* XPS experiments were performed at the ISSIS beamline of the FHI located at the BESSY II synchrotron facility in Berlin, Germany. The high pressure setup consists mainly of a reaction cell attached to a set of differentially pumped electrostatic lenses and a differential-pumped analyzer (Phoibos 150 Plus, SPECS GmbH), as described elsewhere.[30] The spectra were collected in normal emission in vacuum with a probe size of ~ 150 µm x 80 µm. The samples were heated from the back to 180 °C using an external IR-laser (cw, 808 nm) to compensate for charging. The temperature was controlled via a K-type thermocouple in direct contact with the sample surface. Gases were introduced in the reaction cell using calibrated mass flow controllers (Bronkhorst). The gas flows and the products released in the gas phase were simultaneously monitored by a differentially pumped quadrupole mass spectrometer (Pfeiffer) connected via a leak valve to the experimental cell. Sample contamination was checked by survey spectra at the beginning of each experiment. The photoelectron spectra were taken at photon energies of 480, 680 and 780 eV (Pd3d) as well as 680 eV (O1s) and 425 eV (C1s), respectively, with a spectral resolution of 0.3 eV. The low electron kinetic energies of the Pd3d, O1s and C1s regions correspond to an electron mean free path of ≈ 8 Å while the higher electron kinetic energies of the

Pd3d region corresponds to ≈ 10 Å. The total XPS information depth is ≈ 2 nm and 3nm, respectively, that is, 95% of all detected electrons originate from 3λ.[31] For XPS analysis, the photoelectron binding energy (BE) is referenced to the Fermi edge, and the spectra are normalized to the incident photon flux. Background correction was performed by using a Shirley background.[32] The spectra were fitted following the Levenberg-Marquardt algorithm to minimize the χ^2. Peak shapes were modeled by using asymmetric Doniach-Sunjic functions convoluted with Gaussian profiles.[33] The accuracy of the fitted peak positions is ≈ 0.05 eV.

2.9 Ultraviolet photoelectron spectroscopy (UPS). UPS and work function measurements were performed using a Specs Phoibos NAP-150 hemispherical analyzer with a monochromated Al K-alpha source and a non-monochromated He I-alpha ultraviolet source. During the UPS and WF measurements, the sample was held at a bias voltage of -20 V relative to the spectrometer to accelerate the slow secondary electrons. The sample geometry was with the sample normal parallel to the electrostatic lens axis of the analyzer. Samples were measured at temperatures of 100 °C to 450 °C in 50 °C increments. The position of the work function was determined from the secondary electron cut-off, by fitting a line tangent to the data at point of steepest descent, and extrapolating the line to the intersection with the abscissa. The binding energy of this intersection represents the secondary electron cut-off. A value of 20 eV was added to this binding energy to account for the applied voltage, and the resulting number was subtracted from the photon energy to yield the work function.

2.10 Density functional theory (DFT). Plane-wave density functional theory calculations were performed using the Vienna ab initio simulation package (VASP)[34] to calculate the interaction energies between Pd particles and the carbon supports, as well as the reaction coordinates for cinnamaldehyde hydrogenation. In order to fully capture the electronic phenomena occurring at

the metal-carbon interface and their attenuation with distance from the support, the calculations were performed for Pd clusters of 119 and 293 atoms, which corresponds to nanoparticles of 1.7 and 2.5 nm in diameter, respectively and 0.9 and 1.1 nm in height, respectively. The particles were modeled as cubo-octahedral particles which are composed of (100) and (111) surfaces, with atoms arranged in 4–5 metal layers orthogonal to the carbon surface. The support was modeled as either a graphene sheet or a functionalized, defective, graphene sheet (which has 0.125 ML of O* and 0.125 ML of OH* bound to the surface). Carboxylic acid groups were not considered here as these thermolabile groups decompose at low temperature. Therefore, their presence and contribution after catalyst synthesis were ruled out. The lattice parameters for the functionalized graphene sheet were 8.702 and 2.512; those for an equivalent pure graphene sheet were 8.523 and 2.46, indicating that functionalization of the graphene sheet is associated with an expansion in C–C bonds. The functionalized graphene sheet, furthermore, is curved in a periodic manner, further increasing C–C bond lengths in a manner consistent with the rehybridization of C-atoms from sp^2 to sp^3.

Plane-waves were constructed using an energy cutoff of 400 eV with projector augmented wave potentials.[35] The revised Perdew–Burke–Ernzerhof (RPBE) form of the generalized gradient approximation (GGA) was used to determine exchange and correlation energies.[36, 37] Wavefunctions were converged to within 10^{-6} eV and forces were computed using a fast Fourier transform (FFT) grid with a cutoff of twice the planewave cutoff. A 1 × 1 × 1 Γ-point sampling of the first Brillouin zone (k-point mesh) was used and structures were relaxed until forces on unconstrained atoms were <0.05 eV $Å^{-1}$. Converged wavefunctions were transformed into a set of localized quasiatomic orbitals (QUAMBOs)[38] and used to carry out Löwdin population analyses[39] to determine the charges on the individual atoms.

3. RESULTS AND DISCUSSION

3.1 Structural characterization of the Pd/CNT Catalysts. Carbon nanotubes (CNTs) were specifically chosen as the scaffold for this study because they provide key advantages over other carbon supports for investigating metal-carbon interfacial phenomena and their impact on catalysis.[26] In contrast to conventional carbons, which typically present complex 3-dimensional pore systems, CNTs exhibit a tubular morphology with a single cylindrical ~40 nm mesopore extending along the main axis of the nanotube.[28, 29] Their well-defined shape and smooth surface facilitate the high-resolution imaging of the metal nanoparticles and of the metal-carbon interface (Fig. 1). In addition, the defect structure and surface chemistry of the selected CNTs can be tuned without altering their morphology, specific surface area, and porosity,[28, 40, 41] thereby offering a unique platform for establishing relationships between support structure, surface chemistry, and catalytic activity. Finally, the CNT platform also presents advantages for theoretical calculations as this system can be accurately modeled as a defective graphenic sheet with tunable defect density and surface oxygen-containing groups.

Pd/CNT catalysts were prepared by incipient wetness impregnation using an aqueous solution of palladium nitrate and CNTs previously oxidized with nitric acid (Experimental Section). This technique was specifically chosen in order to minimize the number of chemicals and ligands that may subsequently influence the catalytic activity of the metal sites. Specifically, palladium nitrate decomposes at low temperature, below 200 °C,[42] and typically yields Pd nanoparticles free of any inorganic contaminants.[43] Upon reduction in H_2, Pd^0 nanoparticles with an average particle size of 4.14 nm were found to homogeneously decorate both the external and internal surfaces of the CNTs (Fig. 1 and Fig. S1-S2). XRD (5.1 ± 0.3 nm) and H_2 chemisorption (4.57 nm) results were consistent with the average particle size determined from ac-STEM-HAADF images, which

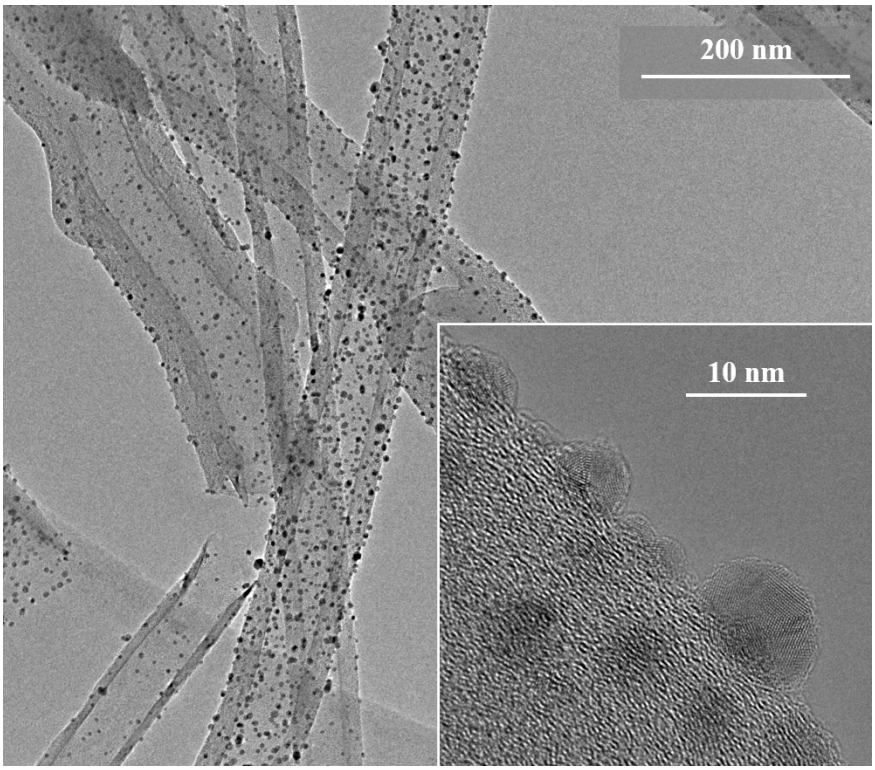

Fig. 1 | Microstructure of the carbon platform and studied catalysts. Transmission electron microscopy image of the Pd/CNT catalyst reduced at 400 °C depicting the dispersion of the Pd nanoparticles (in black) on the CNT surface. **Inset,** high resolution image of Pd-decorated carbon surface. Wavy basic structural carbon units similar to those found in activated carbon and carbon blacks can be clearly seen in black; this similarity emphasizes that the CNT platform accurately models conventional carbon surfaces. Pd atoms clearly follow the topology of the defective surface, indicating strong interfacial interactions.

confirmed that the particles are single crystalline and that their surface was unincumbered by impurities and/or carbon fragments from the support (Tables S1-S2, Fig. S3). Subsequent annealing of the Pd/CNT catalyst in nitrogen at 400, 550, 700, and 850 °C allowed to increase the Pd particle size from 4.14 to > 20 nm (Table S2, Figs. S3-S4) and study the effect of particle size on EMSI and catalytic activity (*vide infra*).

3.2 Evidence for electronic metal-carbon support interactions and interfacial charge redistribution. The decomposition of the nitrate precursor and palladium reduction to Pd^0 were

first investigated by *in situ* NAP-XPS using synchrotron radiation. To this end, the synthesized catalyst precursor $Pd(NO_3)_2$/CNT was introduced in the NAP-XPS chamber, calcined in 0.3 mbar of oxygen at 250 °C, cooled down in vacuum, then treated in 0.3 mbar of hydrogen at 40 °C, and ramped to 400 °C at 10 °C/min to reproduce the conditions used in laboratory experiments. The calcination step decomposed the palladium precursor, leaving Pd atoms in various oxidation states on the scaffold's surface (Fig. S5). The reduction under H_2 converted the metal oxides to metallic Pd^0, as confirmed by the almost complete disappearance of PdO signal at 336.6 eV in the Pd3d spectra (Figs. 2a and S5), and the sharp drop in signal at 530.2 eV in the O1s spectra (Fig. S5). The main Pd3d contribution at 335.1 eV was consistent with the binding energy reported in the literature for bulk Pd^0 (Fig. 2a).[44] However, an additional signal at 335.6-335.65 eV was needed to fit the spectra. This binding energy is inconsistent with the values reported for Pd^+ (~335.5 eV) and Pd^{2+} (336.3-336.9 eV), for both Pd carbides and oxides.[45] In addition, the chemical shift for the $3d_{5/2}$ core level is +0.5-0.55 eV, which is significantly higher than the +0.18-0.29 eV observed for Pd hydride.[45, 46] The valence band spectra also lacked the states with substantial *d* character at 8 eV that were reported for PdH.[47] Therefore, this additional signal was assigned to a charge-depleted palladium phase $Pd^{\delta+}$.

The $Pd^0/Pd^{\delta+}$ ratio calculated from the contributions at 335.1 eV and 335.6-335.65 eV increased from 3.0 to 4.9 over the course of the *in situ* NAP-XPS experiment, indicating a significantly higher metallic character of the Pd phase as the temperature reached 400 °C (Fig. 2a). Interestingly, the $Pd^0/Pd^{\delta+}$ ratio reverted back to 2.2 during cooling in H_2. As the atmosphere inside the NAP-XPS chamber was free of oxygen during cooling to 30 °C and as there was no indication of Pd oxide formation in the O1s spectra (Fig. S5), these results support the presence of a $Pd^{\delta+}$ phase that

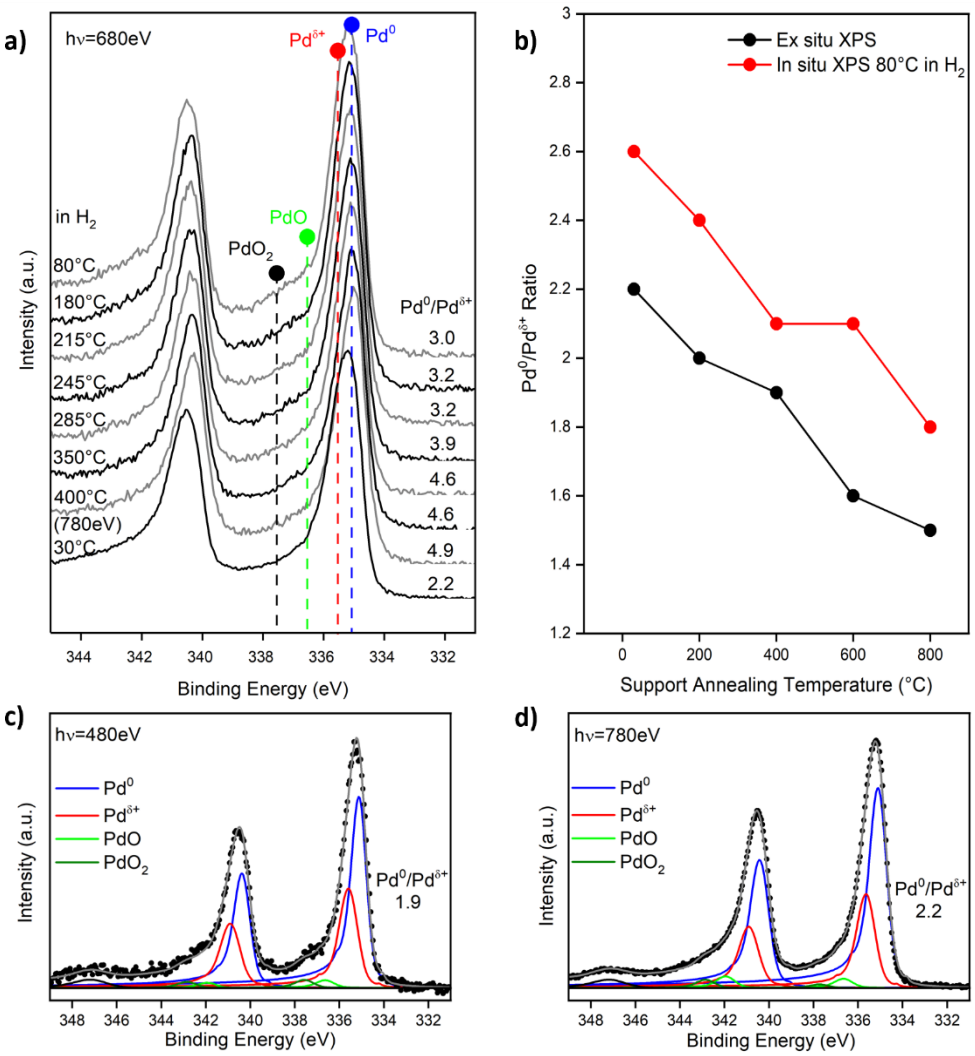

Fig. 2 | *in situ* NAP-XPS investigation of palladium supported on carbon. a, Synchrotron XPS Pd3d spectra of the $Pd(NO_3)_2$/CNT catalyst precursor collected after *in situ* calcination in 0.3 mbar O_2, cooling down to room temperature, and switching to 0.3 mbar H_2. The spectra were collected while heating the sample in H_2 to 400 °C at 10 °C/min and cooling it down to 30 °C upon reduction. The $Pd^0/Pd^{\delta+}$ ratio corresponding to each spectrum is provided on the right side of the spectrum. Note that the bottom spectrum was taken at hν=780 eV and is displayed with fits in Fig. 2d. **b**, Evolution of the $Pd^0/Pd^{\delta+}$ ratio with support functionalization. Oxidized supports were partially defunctionalized through annealing in Argon at 200, 400, 600, and 800 °C prior to $Pd(NO_3)_2$ deposition. The obtained catalysts precursors were subsequently investigated by *in situ* NAP-XPS using the same protocol as for Fig. 2a. The data points correspond to the $Pd^0/Pd^{\delta+}$ ratios calculated from spectra collected upon cooling to 30 °C in H_2. The corresponding *ex situ* XPS results from ref. [26] are indicated for comparison. **c**,**d**, XPS depth profiling spectra collected at the end of the experiment shown in Fig. 2a. The $Pd^0/Pd^{\delta+}$ ratio for each analysis depth is provided next to the corresponding spectrum.

arises from a charge redistribution at the Pd-C interface and that may be influenced by the concentration of oxygen-containing functional groups decorating the scaffold's surface.

Additional experiments were conducted to further study the effect of the support's surface chemistry on the $Pd^{\delta+}$ phase. Oxidized CNTs were partially defunctionalized at 200, 400, 600, and 800 °C prior to Pd nitrate deposition and the obtained samples were investigated by *in situ* NAP-XPS following the same protocol as for $Pd(NO_3)_2$/CNT. The Pd3d spectra acquired upon cooling to 30 °C in H_2 revealed that the $Pd^0/Pd^{\delta+}$ ratio actually decreases from 2.6 to 1.8 with increasing support annealing temperature, in good agreement with *ex situ* XPS results for similar samples (Fig. 2b).[26] Therefore, it can be concluded that the $Pd^{\delta+}$ phase and the corresponding charge transfer at the Pd-C interface are sensitive to both temperature and the O-containing functional groups decorating the defective carbon support.

To elucidate whether the experimentally detected $Pd^{\delta+}$ phase is solely present near the interface or is more broadly distributed, *e.g.* forming a shell around a Pd^0 core, the sample reduced *in situ* (during NAP-XPS) was further investigated using XPS depth profiling by varying the energy of the incident photons from 780 eV to 480 eV, which corresponds to an analysis depth of 1.0 and 0.8 nm, respectively (Figs. 2c,d). Deconvolution of the corresponding spectra revealed an increase in the $Pd^0/Pd^{\delta+}$ ratio from 1.9 to 2.2 with increasing analysis depth, consistent with strong interfacial phenomena that decay with increasing distance from the support. These electronic effects are significant near the interface as they alter the atom's core electrons and induce a perturbation similar to a change in oxidation state. Last, it is worth noting that the XPS depth profiling results were incompatible with a $Pd^{\delta+}$ phase arising from Pd single atoms and/or small clusters. The absence of single atoms was also confirmed here using ac-STEM-HAADF (Fig. S1),

and by Castro Contreras et al. for a series of Pd/C samples synthesized under similar conditions as our Pd/CNT samples. (Fig. S1).[48]

3.3 Consequences of EMSI effects on palladium's catalytic activity. Next, we investigated the effects of this interfacial charge transfer on the reaction rate. To this end, Pd/CNT was annealed in nitrogen for 30 min at temperatures ranging from 400 to 850 °C to tune the metal particle size. Admittedly, this approach alters both the particle size and the support's surface functionalization, which makes it difficult to draw any conclusion from this set of experiments alone. However, alternative approaches for tuning the particle size involving variations in metal loading or ligand-based synthesis were not considered due to other challenges associated with these techniques, such as steric effects of the ligands and possible contamination of the samples with heteroatoms.[49, 50]

Comparing the reaction rates of the obtained catalysts at 10% cinnamaldehyde (CALD) conversion, under kinetically controlled conditions (Supporting Information, equations S1-S38), revealed a strong dependence on the particle size obtained from hydrogen chemisorption (Fig. 3a). The observed drop in the rate cannot be explained by geometric effects (changes in metal surface area) as normalizing the results with the Pd surface area only had a marginal effect on the trend (Fig. S6). These differences in rates were not a result of variations in palladium loading either, as elemental analysis confirmed that the metal loading was uniform across all samples (Table S1). This result was intriguing as cinnamaldehyde hydrogenation was shown to be structure insensitive.[51, 52] Specifically, the turnover frequency (TOF) is unaffected by the particle size for 5-15 nm Pd and Pt nanoparticles decorating an inert support such as silica.[51, 52] At high annealing temperature (850 °C), the drop in reaction rate may be explained by the partial encapsulation of the metal nanoparticles with carbon, as observed by ac-TEM (Fig. S4). It appears that carbon atoms

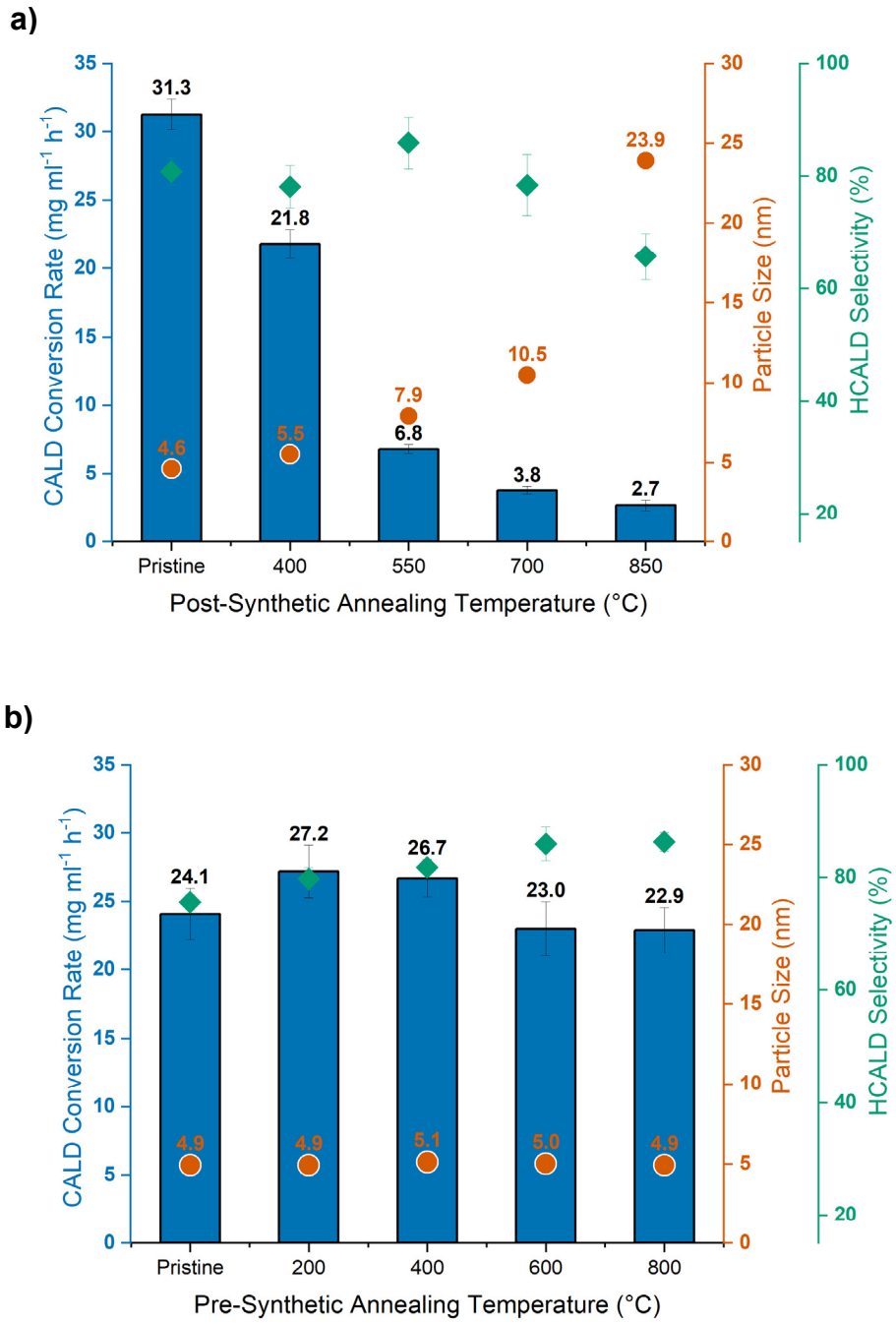

Fig. 3 | Effect of annealing pre and post palladium deposition on catalytic activity. a, CALD conversion rate decreases with treatment temperature for Pd/CNT catalysts annealed at different temperatures after Pd deposition (post-synthetic annealing). The HCALD (hydrocinnamaldehyde) selectivity remains unaffected while the Pd particle size increases with annealing temperature. **b,** The CNTs were annealed prior to Pd metal depositions for the pre-synthetic annealing series, which resulted in consistent CALD conversion rates and Pd particle sizes across the series. The HCALD selectivity demonstrates an increasing trend with support annealing temperature.

from the defective support become mobile at high temperature, above 800 °C, and migrate onto the metal nanoparticles. This phenomenon also explains the overestimation of the metal particle size by chemisorption compared to XRD for this sample (Table S2). However, at lower annealing temperatures, the metal surface was found to be free of carbon and the observed drop in normalized rates was free from artifacts.

To determine the independent role of support functionalization, a separate set of experiments was performed where the oxidized CNTs were annealed in an inert atmosphere *prior* to Pd deposition (Fig. 3b). For this sample series, the Pd particle size was kept constant at 4.9-5.1 nm and, therefore, support functionalization was the only variable that could alter the catalytic performance. As can be seen in Figure 3b, the CALD conversion rate remained within experimental error, independently of the support's annealing temperature, for this sample series. These results suggest more complex support effects in Figure 3a that solely take place at the Pd-C interface and that are directly correlated to the area of the metal-carbon contact. The impact of these supports effects on reaction rate and selectivity are further discussed in Sections 3.4 and 3.6, respectively.

3.4 Spatial distribution of the $Pd^{\delta+}$ phase and contribution to the observed change in reaction rate. To further probe the spatial distribution of the $Pd^{\delta+}$ phase and understand its contribution to the trend in reaction rate observed in Figure 3a, we developed a simple model based on the hemispherical particle shape observed by TEM and the average Pd particle size measured by hydrogen chemisorption, using Equations S39-S44 (Supporting Information). This model served to analyze the scaling relationship between particle size and the number of active sites located on the nanoparticle's surface and near the Pd-C interface. As can be seen in Figure 4a, the

number of surface sites per volume is proportional to the diameter d of the metal nanoparticle as d^{-1} while the number of sites at the circumference drops as d^{-2}. The turnover frequencies (TOF) calculated for Pd/CNT and the samples post-synthetically annealed at 400, 550, and 700 °C where then plotted in the same graph (black curve in Fig. 4a). The sample annealed at 850 °C was not included in this analysis as TEM revealed that part of the nanoparticles' surface was covered with carbon, thus causing errors both in the initial rate measurements and the metal surface area obtained from H_2 chemisorption (*vide supra*). As the experimental TOFs showed a dependence of the nanoparticles' diameter as $\sim d^{-1.7}$, the sites at or near the metal-support interface drive the reaction kinetics.[53]

When combined with the results of the NAP-XPS depth profiling (Fig. 2c,d), this observation suggests an interfacial $Pd^{\delta+}$ phase with a higher intrinsic rate (TOF) than the Pd^0 phase further away from the carbon scaffold. To test this hypothesis, the model was refined assuming this time $Pd^{\delta+}$ atoms organized in a spherical frustum of radius R and height x covered by a spherical cap of Pd^0 atoms with a radius (R-x), as shown in Fig. S7. Using the $Pd^0/Pd^{\delta+}$ ratio calculated from the Pd3d spectrum of the Pd/CNT sample, the effective range of the $Pd^{\delta+}$ atoms was found to be 0.45-0.57 nm (Eq. S45-47). Considering the limitations of XPS, it is reasonable to assume that this value corresponds to 1–2 atomic layers (0.27-0.66 nm) of $Pd^{\delta+}$, which is consistent with the scaling relation established from Fig. 4a. This scaling relation also suggests that the $Pd^{\delta+}$ atoms, or those near them, create a perimeter of highly active sites at the interface, and an equation was subsequently derived (Eq. S50) and applied to determine the intrinsic rates of sites near the interface and residual sites further away from the carbon support through nonlinear regression analysis (Fig. 4b, model 2). Sites near the interface ($Pd^{\delta+}$ and nearby atoms) were found to be 50-200 times more active than Pd^0. In comparison, a model assuming the same intrinsic rate for

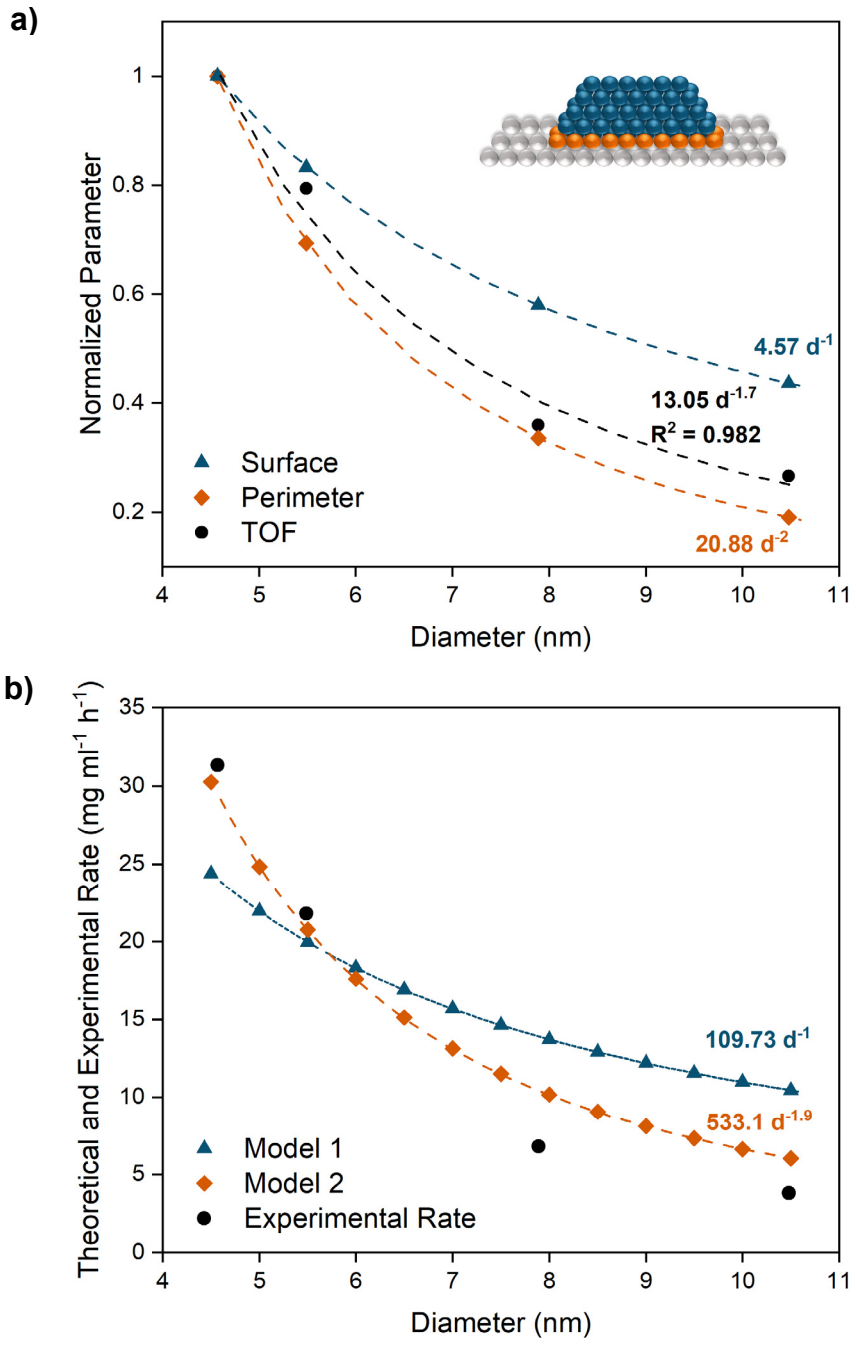

Fig. 4 | Relationship between reaction kinetics, particle size, and location of the active sites. **a,** Experimental turnover frequency (TOF) and calculated number of sites at the perimeter (orange) and surface (blue) as a function of Pd particle size. The TOFs were calculated based on the rates in Fig. 3a. All data were normalized using the highest value of each parameter for easier comparison. **b,** Fitting of the measured reaction rates (black circles) using two models that assume that all atoms have the same intrinsic reaction rate (model 1, in blue) or that atoms at the interface with the carbon support and at the surface present different intrinsic rates (model 2, in orange).

interfacial and non-interfacial sites gave a rather poor fit regardless of the value chosen for the rate (Fig. 4b, model 1).

3.5 Theoretical insights into reactions at the Pd-C interface. Turnover rates correlate with particle diameter (TOF $\propto d^{-2}$) in a manner that suggests interfacial sites are predominantly active for this reaction, and XPS data suggests a thin region (1-2 metal layers) of $Pd^{\delta+}$ atoms at the Pd-C interface. However, the influence of $Pd^{\delta+}$ atoms (and those they neighbor) on adsorbate binding energies and chemistry is not directly known from these experimental studies. Therefore, DFT calculations were performed to examine adsorbates and reactions on Pd_{119} and Pd_{293} hemispherical cubo-octahedral particles supported on functionalized graphene supports, used here as a model surface consistent with the structure and surface chemistry of the CNTs.

Metal surfaces are often treated as a series of non-interacting sites by Langmuirian models, in direct contrast to the well-described effects of particle size and shape on turnover rates.[54, 55] These effects of particle morphology are typically described as altering a distribution of metal atoms in low-index terraces, undercoordinated edge and corner sites, and in step-edge defect sites.[54, 56, 57] Surface-support interactivity is often attributed to reactants converting directly at metal-support interfaces, often transferring from the support to the metal.[58-60] Here, our DFT calculations revealed a new type of heterogeneity among metal surface sites by demonstrating that metal atoms in low-index planes are directly affected by their proximity to the underlying support—even for reactions that do not directly react with or bind to support atoms.

The average binding energies of CH*, O*, and H* (Fig. 5, with Figs. S8-S12 showing individual binding energy maps) vary with position and proximity to the supports (modeled as graphene sheets and graphene functionalized by O* and OH* groups, as described in Supporting

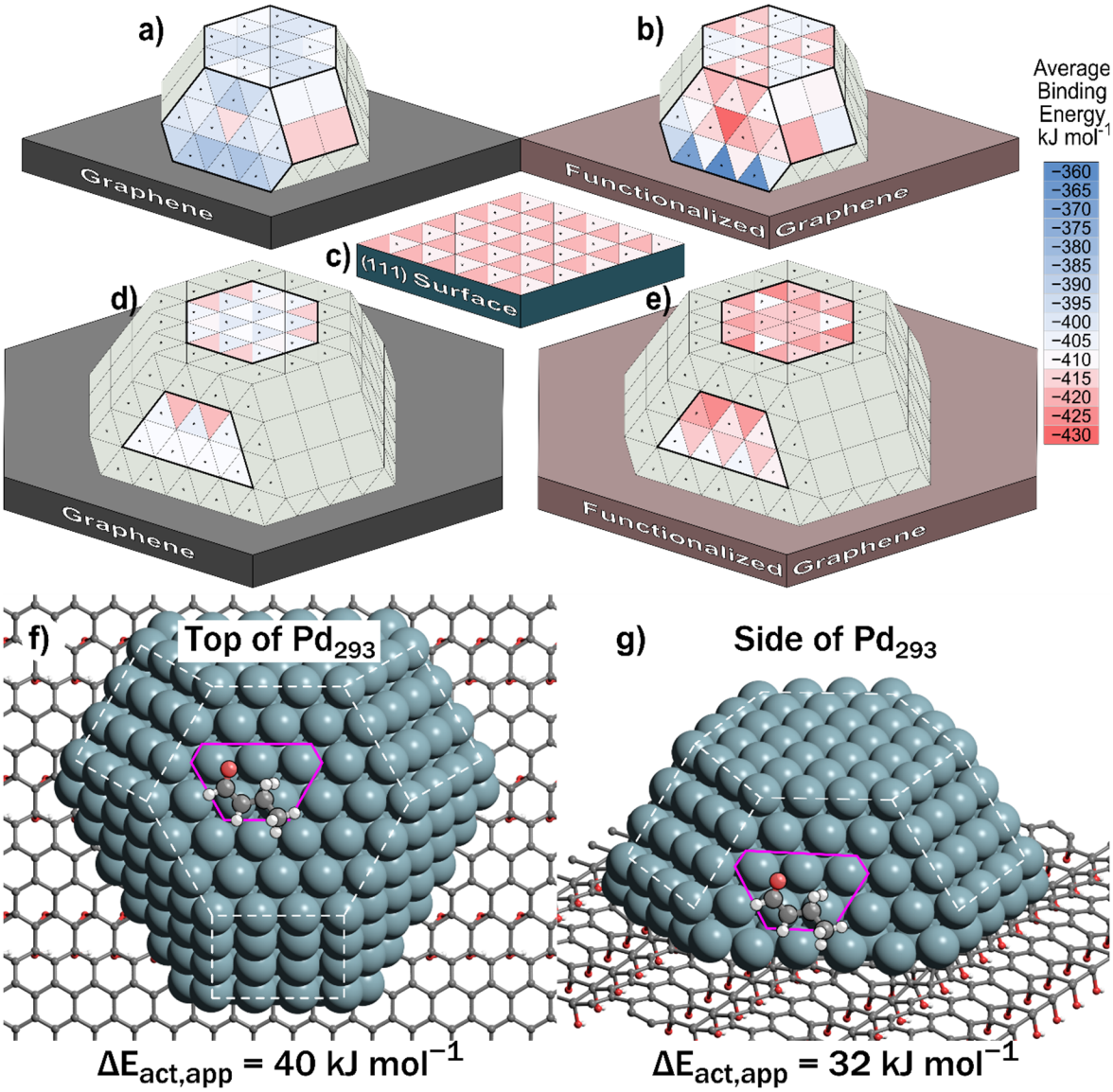

Fig. 5 | DFT models and computed binding energies for various metal sites. Average binding energy (kJ mol^{-1}) for CH*, O*, and H* on a Pd (111) surface (**c**), as well as Pd_{119} (**a** and **b**) and Pd_{293} (**d** and **e**) clusters on pristine (**a** and **d**) and functionalized (**b** and **e**) graphene supports. Dots indicate three-fold hcp sites, other sites are three-fold fcc on the (111) surface or four-fold hollow on the (100) surface. Gray-green coloring indicates unexamined binding sites. Blue-red coloring indicates binding energies. Similar figures for individual CH*, O*, and H* binding energies are shown in the Supporting Information (Figs. S8-S12). Apparent activation energies (relative to gas phase crotonaldehyde) for the first C–H bond formation on top (**f**) and the side (**g**) of a Pd_{293} cluster on functionalized graphene.

Information) on Pd_{119} and Pd_{293} particles. These three adsorbates always bind to three-fold or four-fold hollow sites on (111) and (100) facets and describe how many hydrocarbons and oxygenates bind via scaling relationships.[61] CH*, O*, and H* adsorbed slightly stronger to Pd particles on functionalized graphene (−407 kJ mol^{-1}) than to Pd particles on pristine graphene (−401 kJ mol^{-1}) across the same ensemble of binding sites, with sites differently impacted by the underlying support depending on their proximity to the interface. The binding properties of these metal sites were not only influenced by the metal-atom coordination of their ensembles but also by the identity of the underlying support. For example, the average binding energy for CH*, O*, and H* in a three-fold fcc site on the top of the graphene-supported Pd_{119} is −403 kJ mol^{-1}, whereas the same site on the functionalized graphene-supported particle binds these species with an average energy of −416 kJ mol^{-1} (Figs. 5a,b). Similar results are observed for three-fold fcc sites on top of Pd_{293} particles, with average binding energies of −413 kJ mol^{-1} for graphene-supported Pd_{293} and −420 kJ mol^{-1} for functionalized graphene-supported Pd_{293} (Figs. 5d,e). These data indicate that the electron-withdrawing effects of the functionalized graphene support cause Pd surface atoms four or five metal-atom layers away to bind species more strongly by an average of 8 kJ mol^{-1} for CH*, O*, and H* adsorbates. Therefore, the "size" of the interfacial region is larger than a single row of metal atoms. Large changes in the support (contrasting non-interacting graphene and strongly interacting functionalized graphene) can be felt up to 4-5 metal layers away.

The proximity between the support and the binding site also impacts site reactivity. For example, three-fold fcc sites on top of Pd_{119} particles have average binding energies of −403 kJ mol^{-1} and −416 kJ mol^{-1} on pristine and functionalized graphene-supported particles, respectively. Whereas three-fold fcc sites on the sides of Pd_{119} particles have average binding energies of −414 kJ mol^{-1} and −428 kJ mol^{-1}, respectively, or ~10 kJ mol^{-1} lower than sites on top of the metal

particle (Fig. 5). These shifts are not caused by changes in the metal atom coordination as these sites do not include corner/edge metal atoms. $Pd^{\delta+}$ atoms directly bound to the functionalized graphene support bind CH*, O*, and H* significantly more weakly than non-interfacial sites (Fig. 5b), which indicates that the enhanced reactivity of catalysts with greater $Pd^{\delta+}$ intensities is caused by the influence that $Pd^{\delta+}$ atoms have on their neighboring sites. In other words, XPS data and DFT-based charge analysis of Pd-C interfaces suggest a thin perimeter of $Pd^{\delta+}$ atoms is varied by the degree of C-support functionalization as tuned by the annealing treatments. DFT calculations of adsorbate binding energies suggest that Pd atoms near this perimeter of $Pd^{\delta+}$ bind adsorbates more strongly, leading an increase in the amount of irreversibly bound H* during H_2 chemisorption.

To test the role of these near-interfacial sites on hydrogenation chemistry, we then examined the H*-addition to crotonaldehyde (but-2-enal), a model *α,β*-unsaturated compound and a cinnamaldehyde proxy; this simpler model compound allows for a closer assessment of the effects of support and location on its hydrogenation without steric influences of the phenyl group. Crotonaldehyde can form two primary products (butanal and butenol) from hydrogenation, similar to the two distinct enol and aldehyde primary products that are formed in cinnamaldehyde hydrogenation. Reactivity trends observed for cinnamaldehyde hydrogenation on Pd/C catalysts suggest that C=C bonds are selectively hydrogenated at low conversions. Crotonaldehyde hydrogenation was modeled to complete saturation (forming 1-butanol) on Pd(111) surfaces to determine kinetically-relevant steps in the formation of butenal and in the direct formation of 1-butanol. Activation and reaction free energies suggest that butenal is formed via sequential H-addition to the C3 atom (adjacent to the $–CH_3$ group) followed by H-addition to the C2 atom; in which the first H-addition (to C3) is the rate determining step. This reaction was then modeled

on top of the Pd_{293} cluster and near the metal-support interface (without directly binding to that interface). All symmetrically unique metal ensembles were considered. The apparent activation barrier for H-addition to crotonaldehyde was 40 kJ mol^{-1} when the reaction was modeled on top of the Pd_{293} particle; however, when this same reaction was modeled on the side of the same Pd_{293} particle on functionalized graphene, the apparent barrier was 32 kJ mol^{-1}. This decrease in the activation barrier by 8 kJ mol^{-1} for reactions occurring near the interface is consistent with increased reactivity of those sites as inferred from kinetic data in previous sections. The transition states used to calculate these barriers do not involve edge/corner atoms or Pd atoms bound directly to the support and do not consider palladium hydrides, and thus this shift only represents the impacts of proximity between the metal ensemble and the underlying carbon support.

The heterogeneity of a metal surface is caused by the distinct crystal facets (e.g. (111) vs (100)), the metal-atom coordination of the binding ensemble, and the proximity to the underlying support. The proximity effects are demonstrated here for large metal particles (>100 atoms) on a non-covalently and covalently interacting carbon supports. The support can shift binding energies of small model adsorbates (CH*, OH*, and H*) as well as alter activation barriers for key reactions, and thus the support may influence rates without directly binding to or interacting with reacting species. These electronic effects may be screened for many sites on large metal particles, but sites near the interface will be influenced by carbon supports for any particle size, even if those sites are not directly at the interface. Overall, the calculations confirm that the metal-support charge transfer creates $Pd^{\delta+}$ atoms, alters the intrinsic rate of $Pd^{\delta+}$ atoms and sites near the $Pd^{\delta+}$ atoms, and explains the drop in TOF with increasing particle size (Fig. 4). The calculations all support the increase in TOF with increasing number of $Pd^{\delta+}$ atoms, hence greater Pd-carbon support interactions.

3.6 Elucidation of the driving forces behind the charge redistribution at the Pd-C interface.

The annealed Pd/CNT samples were critical to establish correlations between reaction rate and location of the active sites. However, we found these samples were unsuitable for elucidating the origin of the EMSI effects as post-synthetic annealing simultaneously alters the Pd particle size and the support's surface functionalization. Conversely, the pre-synthetically annealed samples were ideal as annealing was performed prior to Pd deposition and the particle size across all catalysts in this series was consistent (~ 5nm). Moreover, supports (without Pd) and catalysts can be thoroughly characterized to establish correlations between the scaffold's surface chemistry (O/C ratio), its electronic properties, their effect on the Pd phase ($Pd^0/Pd^{\delta+}$ ratio), and performance of the final catalyst.

Using a laboratory setup equipped for both XPS and UPS, we simultaneously monitored the temperature-dependent changes in surface composition of the oxidized CNTs using XPS and changes in their work function (WF) using UPS.[62] The data collected for the pristine CNTs during annealing to 450 °C in 50 °C intervals is presented in Figure 6a. The various oxygen-containing groups that decorate the CNT surface thermally decomposed during the annealing process, causing a drop in the O/C ratio from 0.12 to 0.08 (Table S3). This defunctionalization was accompanied by a linear decrease in the WF from 4.80 eV to 4.48 eV (Fig. 6a). This trend is consistent with prior studies on reduced graphene oxide by Yang et al.[62] and Sygellou et al.[63] Surface oxygen-containing functional groups act as dipoles that alter the electronic structure of graphitic carbons causing an upshift of the WF from ~4.2 eV for graphite to ~5.3 eV for highly functionalized graphene oxide. Fig. 6a demonstrates that the CNTs used in the present study offer a unique platform for studying and understanding EMSI effects in carbon-supported catalysts. In contrast

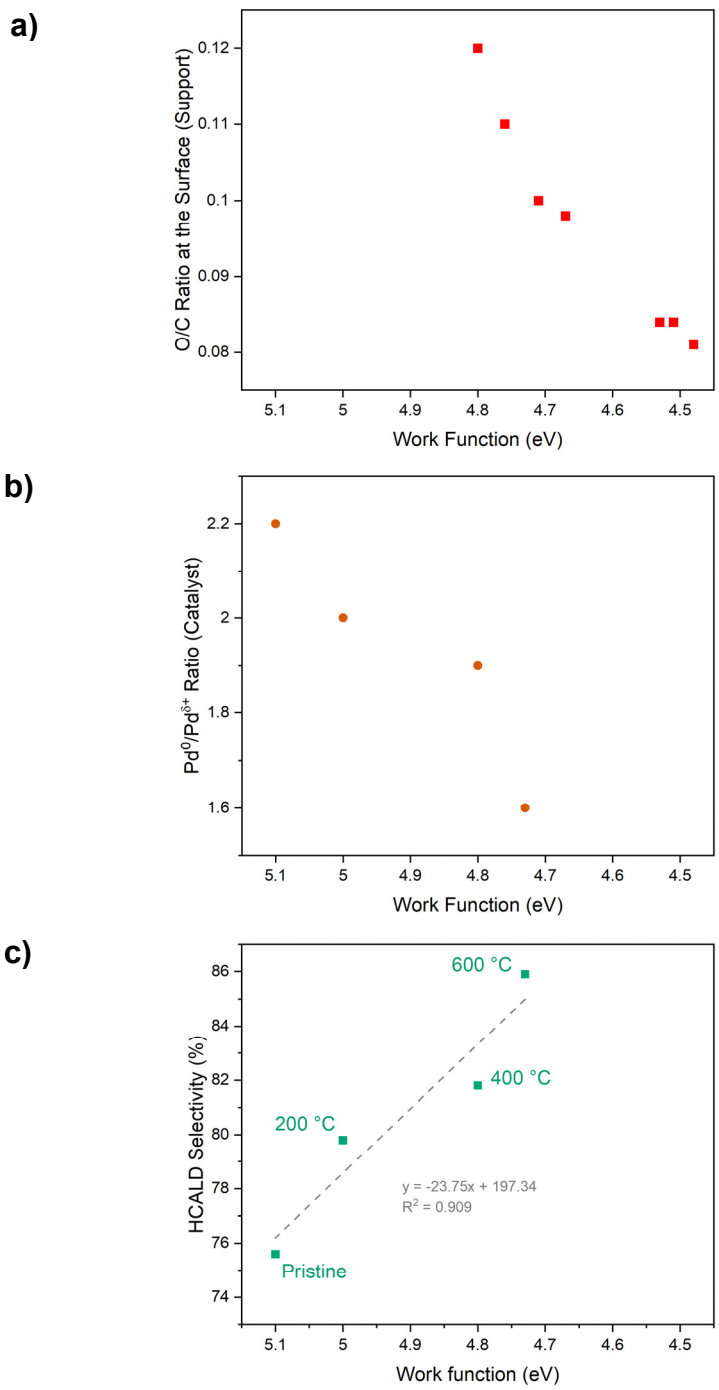

Fig. 6 | Correlations between support functionalization, interfacial charge transfer, and catalyst performance. a, Trend between surface O/C ratio of the support from XPS and work function from UPS for the oxidized CNT support annealed *in situ* from 100 to 450 °C by 50 °C increments. **b**, Correlation between the $Pd^0/Pd^{\delta+}$ ratio determined by XPS and the work function from UPS for the pre-synthetically annealed Pd/CNT catalyst series. **c**, Linear trend between the work function of the catalysts and their selectivity towards HCALD; the data points correspond to the same catalysts as in (**b**).

to other carbon supports, the CNTs' surface chemistry and WF can be carefully tailored while keeping other important variables such as surface area and porosity constant.

The corresponding pre-synthetically annealed Pd/CNT catalysts were subsequently studied using a similar approach (Fig. 6b). For this set of samples, we first confirmed that the nitrate metal precursor did not cause any reoxidation of the carbon surface during catalyst synthesis (Table S4). Such a reoxidation was observed for Co/CNT catalysts, *albeit* for much higher metal loadings.[64] The combined XPS/UPS analysis of the $Pd(NO_3)_2$/CNT precursor showed a rapid drop of the O/C ratio from 0.21 to 0.12 when heating the sample to 200 °C. The latter is close to the O/C ratio of 0.11 obtained for the oxidized CNTs when defunctionalized at the same temperature. The WF measured for the oxidized CNTs and Pd/CNT after annealing at 200 °C were also consistent (5.0 eV). Next, we focused our attention on the changes in the $Pd^0/Pd^{\delta+}$ ratios calculated from the Pd3d spectra with increasing annealing temperature and their relationship with the catalysts' WF (Fig. 6b, Tables S3 and S5). Interestingly, the $Pd^0/Pd^{\delta+}$ ratio showed the same linear relationship with the catalyst's WF than between the O/C ratio and the scaffold's WF (Fig 6a), which further supports that the $Pd^{\delta+}$ arises from EMSI effects that scale with the CNT's surface functionalization, hence its electronic properties as revealed by the WF. Therefore, our results
suggest that the $Pd^{\delta+}$ phase observed by XPS arises from the difference in position of the Fermi levels of functionalized carbon supports and palladium nanoparticles.

Last, a linear correlation between the catalyst's selectivity towards HCALD and the WF was observed as well (Fig. 6c), which further strengthened the trends between the support's electronic properties and the catalytic performance of the metal active phase. As the annealing temperature increases, the carbon surface is progressively defunctionalized which causes a downshift of the support's WF. As a result, the difference in energy between the work functions of palladium and

the carbon support increases, which enhances the interfacial EMSI effects and, therefore, the charge transfer from the interfacial Pd atoms to the carbon. This translates into faster kinetics for the hydrogenation of CALD to HCALD and, consequently, a higher selectivity to HCALD.

4. CONCLUSION

In this work, we have demonstrated that carbons are not inert scaffolds, and that they can substantially alter the catalytic activity of the supported metal active phase through charge transfer at the metal-carbon interface, *i.e.* through EMSI effects. These EMSI effects are strong enough near the interface to shift the binding energy of palladium atoms' core electrons by 0.5-0.55 eV. As this shift is of the same order of magnitude as a change in oxidation state, we followed the calcination-reduction process by *in situ* NAP-XPS using synchrotron radiation. These experiments provided direct evidence that the Pd nitrate precursor decomposes at low temperature to form PdO in oxygen and is reduced to form ~5 nm metallic Pd nanoparticles in hydrogen. NAP-XPS confirmed that, in contrast to Pd on oxide supports, a substantial fraction of the Pd atoms remain in a $Pd^{\delta+}$ state, even after reduction at 400 °C in hydrogen. Analysis of the O1s and C1s spectra revealed that Pd oxides and Pd carbides can be excluded under these conditions. In addition, this $Pd^{\delta+}$ phase was also detected in vacuum for conditions under which Pd hydrides are unstable. Depth profiling revealed that in contrast to core-shell structures for which significant changes in composition are detected depending on the analysis depth, the $Pd^0/Pd^{\delta+}$ ratio varied only slightly from 1.9 to 2.2. This result is consistent with a $Pd^{\delta+}$ phase present only at the interface with the carbon support. However, the possible contribution of Pd single atoms to this signal was ruled out based on ac-STEM-HAADF images.

As the samples were annealed and the Pd particle size increased, a larger number of Pd atoms were present in the bulk of the metal nanoparticles. This change in composition altered the rate of the reaction. However, the decrease in rate was inconsistent with simple geometric effects as the turnover frequency dropped with particle size. This observation suggested that the intrinsic rate of the Pd atoms depends on their position in the metal particle and that $Pd^{\delta+}$ atoms near the interface may be significantly more active than Pd^0 atoms. To further test this hypothesis, we developed a simple mathematical model to analyze the scaling relations with particle size. When Pd atoms all show the same intrinsic rate, the overall activity decreases with an inverse 1st order trend inconsistent with the experimental data. Using the $Pd^0/Pd^{\delta+}$ ratio provided by XPS, we then attributed different intrinsic rates to the two phases to change their weighted contributions to the overall reactivity. We found that to fit the experimental data, Pd atoms near the interface must show an intrinsic rate about two orders of magnitude higher than bulk Pd^0 atoms. This intrinsic rate is consistent with the DFT calculations as the energy barrier for butenal hydrogenation to butanal is about 10 kJ mol^{-1} lower for Pd atoms near the interface than for Pd atoms in (111) terraces further away. These results also explain the increase in selectivity observed when supports were annealed prior to Pd deposition. As the $Pd^{\delta+}$ contribution increases with the annealing temperature for this sample series, the formation of hydrocinnamaldehyde is kinetically favored over 3-phenylpropanol due to the lower energy barrier for Pd atoms near the interface.

Finally, we confirmed the presence of EMSI effects using UPS. This technique allows a direct measure of the work function of the catalysts, hereby providing direct evidence for changes in the electronic structure of the support and its effect on the active phase. Although UPS characterizes an integral change in catalyst properties (not just the Pd-C interface), linear correlations between support functionalization, work function, $Pd^{\delta+}$ contribution, and catalyst selectivity are established.

In summary, we demonstrated the existence of EMSI effects for Pd/C that are triggered by oxygen doping and that can be modulated through simple thermal treatments. These effects are strong enough to change the electronic structure of Pd atoms near the interface and, consequently, their adsorption properties and catalytic activity.

AUTHOR INFORMATION

Corresponding Author

* E-mail address: tesso@iastate.edu

Author Contributions

R.G.R conceived the work, performed experiments, and wrote the manuscript. R.B., M.G., P.L. and T.W.H. performed experiments and wrote the manuscript. K.S.D. and D.D.H. performed theoretical calculations and wrote the manuscript. J.-P.T. conceived and supervised the work, secured funding, and wrote the manuscript. All authors have given approval to the final version of the manuscript.

Funding Sources

This material is based upon work supported in part by the National Science Foundation under grant numbers EEC-0813570 and CBET-1804436.

ASSOCIATED CONTENT

Supporting Information. Additional characterizations of the synthesized catalysts by ICP-OES, XRD, H_2 chemisorption, ac-TEM, ac-STEM-HAADF, NAP-XPS, and UPS; detailed internal and external mass transfer analysis; detailed description and equations used to develop the models used in Fig. 4; additional DFT calculations.

ACKNOWLEDGMENT

R.G.R thanks Elspeth Petersen for her help with the NAP-XPS measurements. The authors also thank Dr. Axel Knop-Gericke and Prof. Robert Schlögl of the Fritz Haber Institute for facilitating the NAP-XPS experiments.

REFERENCES

(1) Matsubu, J. C.; Zhang, S.; DeRita, L.; Marinkovic, N. S.; Chen, J. G.; Graham, G. W.; Pan, X.; Christopher, P. Adsorbate-Mediated Strong Metal–Support Interactions in Oxide-Supported Rh Catalysts. *Nat. Chem.* **2017**, *9* (2), 120-127. DOI: 10.1038/nchem.2607.

(2) Mitchell, S.; Qin, R.; Zheng, N.; Pérez-Ramírez, J. Nanoscale Engineering of Catalytic Materials for Sustainable Technologies. *Nat. Nanotechnol.* **2021**, *16* (2), 129-139. DOI: 10.1038/s41565-020-00799-8.

(3) Kumar, G.; Tibbitts, L.; Newell, J.; Panthi, B.; Mukhopadhyay, A.; Rioux, R. M.; Pursell, C. J.; Janik, M.; Chandler, B. D. Evaluating Differences in the Active-Site Electronics of Supported Au Nanoparticle Catalysts Using Hammett and DFT Studies. *Nat. Chem.* **2018**, *10* (3), 268-274. DOI: 10.1038/nchem.2911.

(4) Campbell, C. T. Electronic Perturbations. *Nat. Chem.* **2012**, *4* (8), 597-598. DOI: 10.1038/nchem.1412.

(5) Chen, H.; Shuang, H.; Lin, W.; Li, X.; Zhang, Z.; Li, J.; Fu, J. Tuning Interfacial Electronic Properties of Palladium Oxide on Vacancy-Abundant Carbon Nitride for Low-Temperature Dehydrogenation. *ACS Catal.* **2021**, *11* (10), 6193-6199. DOI: 10.1021/acscatal.1c00712.

(6) Wu, P.; Wu, Z.; Mullins, D. R.; Yang, S.-Z.; Han, X.; Zhang, Y.; Foo, G. S.; Li, H.; Zhu, W.; Dai, S.; et al. Promoting Pt Catalysis for CO Oxidation Via the Mott–Schottky Effect. *Nanoscale* **2019**, *11*, 18568-18574. DOI: 10.1039/C9NR04055B.

(7) Jia, Q.; Ghoshal, S.; Li, J.; Liang, W.; Meng, G.; Che, H.; Zhang, S.; Ma, Z.-F.; Mukerjee, S. Metal and Metal Oxide Interactions and Their Catalytic Consequences for Oxygen Reduction Reaction. *J. Am. Chem. Soc.* **2017**, *139* (23), 7893-7903. DOI: 10.1021/jacs.7b02378.

(8) He, Z.; Dong, B.; Wang, W.; Yang, G.; Cao, Y.; Wang, H.; Yang, Y.; Wang, Q.; Peng, F.; Yu, H. Elucidating Interaction between Palladium and N-Doped Carbon Nanotubes: Effect of Electronic Property on Activity for Nitrobenzene Hydrogenation. *ACS Catal.* **2019**, *9* (4), 2893-2901. DOI: 10.1021/acscatal.8b03965.

(9) Tan, D.; Wulan, B.; Cao, X.; Zhang, J. Strong Interactions of Metal-Support for Efficient Reduction of Carbon Dioxide into Ethylene. *Nano Energy* **2021**, *89*, 106460. DOI: 10.1016/j.nanoen.2021.106460.

(10) Kaiser, S. K.; Surin, I.; Amorós-Pérez, A.; Büchele, S.; Krumeich, F.; Clark, A. H.; Román-Martínez, M. C.; Lillo-Ródenas, M. A.; Pérez-Ramírez, J. Design of Carbon Supports for Metal-Catalyzed Acetylene Hydrochlorination. *Nat. Commun.* **2021**, *12* (1), 4016. DOI: 10.1038/s41467-021-24330-2.

(11) Yan, Q.-Q.; Yin, P.; Liang, H.-W. Engineering the Electronic Interaction between Metals and Carbon Supports for Oxygen/Hydrogen Electrocatalysis. *ACS Mater. Lett.* **2021**, *3* (8), 1197-1212. DOI: 10.1021/acsmaterialslett.1c00266.

(12) Warczinski, L.; Hättig, C. How Nitrogen Doping Affects Hydrogen Spillover on Carbon-Supported Pd Nanoparticles: New Insights from DFT. *J. Phys. Chem. C.* **2021**, *125* (17), 9020-9031. DOI: 10.1021/acs.jpcc.0c11412.

(13) Zhuo, H.-Y.; Zhang, X.; Liang, J.-X.; Yu, Q.; Xiao, H.; Li, J. Theoretical Understandings of Graphene-Based Metal Single-Atom Catalysts: Stability and Catalytic Performance. *Chem. Rev.* **2020**, *120* (21), 12315-12341. DOI: 10.1021/acs.chemrev.0c00818.

(14) Gerber, I. C.; Serp, P. A Theory/Experience Description of Support Effects in Carbon-Supported Catalysts. *Chem. Rev.* **2020**, *120* (2), 1250-1349. DOI: 10.1021/acs.chemrev.9b00209.

(15) Jackson, C.; Smith, G. T.; Inwood, D. W.; Leach, A. S.; Whalley, P. S.; Callisti, M.; Polcar, T.; Russell, A. E.; Levecque, P.; Kramer, D. Electronic Metal-Support Interaction Enhanced Oxygen Reduction Activity and Stability of Boron Carbide Supported Platinum. *Nat. Commun.* **2017**, *8* (1), 15802. DOI: 10.1038/ncomms15802.

(16) Varela, A. S.; Ju, W.; Bagger, A.; Franco, P.; Rossmeisl, J.; Strasser, P. Electrochemical Reduction of CO2 on Metal-Nitrogen-Doped Carbon Catalysts. *ACS Catal.* **2019**, *9* (8), 7270-7284. DOI: 10.1021/acscatal.9b01405.

(17) Toebes, M. L.; Alexander Nijhuis, T.; Hájek, J.; Bitter, J. H.; Jos van Dillen, A.; Murzin, D. Y.; de Jong, K. P. Support Effects in Hydrogenation of Cinnamaldehyde over Carbon Nanofiber-Supported Platinum Catalysts: Kinetic Modeling. *Chem. Eng. Sci.* **2005**, *60* (21), 5682-5695. DOI: 10.1016/j.ces.2005.05.031.

(18) Xiang, Y.; Kong, L.; Xie, P.; Xu, T.; Wang, J.; Li, X. Carbon Nanotubes and Activated Carbons Supported Catalysts for Phenol in Situ Hydrogenation: Hydrophobic/Hydrophilic Effect. *Ind. Eng. Chem. Res.* **2014**, *53* (6), 2197-2203. DOI: 10.1021/ie4035253.

(19) Gosselink, R. W.; Xia, W.; Muhler, M.; de Jong, K. P.; Bitter, J. H. Enhancing the Activity of Pd on Carbon Nanofibers for Deoxygenation of Amphiphilic Fatty Acid Molecules through Support Polarity. *ACS Catal.* **2013**, *3* (10), 2397-2402. DOI: 10.1021/cs400478q.

(20) Wang, X.; Liang, X.; Geng, P.; Li, Q. Recent Advances in Selective Hydrogenation of Cinnamaldehyde over Supported Metal-Based Catalysts. *ACS Catal.* **2020**, *10* (4), 2395-2412. DOI: 10.1021/acscatal.9b05031.

(21) Yang, Y.; Reber, A. C.; Gilliland, S. E.; Castano, C. E.; Gupton, B. F.; Khanna, S. N. More Than Just a Support: Graphene as a Solid-State Ligand for Palladium-Catalyzed Cross-Coupling Reactions. *J. Catal.* **2018**, *360*, 20-26. DOI: 10.1016/j.jcat.2018.01.027.

(22) Yang, Y.; Reber, A. C.; Gilliland, S. E.; Castano, C. E.; Gupton, B. F.; Khanna, S. N. Donor/Acceptor Concepts for Developing Efficient Suzuki Cross-Coupling Catalysts Using Graphene-Supported Ni, Cu, Fe, Pd, and Bimetallic Pd/Ni Clusters. *J. Phys. Chem. C.* **2018**, *122* (44), 25396-25403. DOI: 10.1021/acs.jpcc.8b07538.

(23) Franco, M.; Sainz, R.; Lamsabhi, A. M.; Díaz, C.; Tortosa, M.; Cid, M. B. Evaluation of the Role of Graphene-Based Cu(I) Catalysts in Borylation Reactions. *Catal. Sci. Technol.* **2021**, *11* (10), 3501-3513. DOI: 10.1039/D1CY00104C.

(24) Nie, R.; Jiang, H.; Lu, X.; Zhou, D.; Xia, Q. Highly Active Electron-Deficient Pd Clusters on N-Doped Active Carbon for Aromatic Ring Hydrogenation. *Catal. Sci. Technol.* **2016**, *6* (6), 1913-1920. DOI: 10.1039/C5CY01418B.

(25) Şen, F.; Gökağaç, G. Different Sized Platinum Nanoparticles Supported on Carbon: An Xps Study on These Methanol Oxidation Catalysts. *J. Phys. Chem. C.* **2007**, *111* (15), 5715-5720. DOI: 10.1021/jp068381b.

(26) Rao, R. G.; Blume, R.; Hansen, T. W.; Fuentes, E.; Dreyer, K.; Moldovan, S.; Ersen, O.; Hibbitts, D. D.; Chabal, Y. J.; Schlögl, R.; et al. Interfacial Charge Distributions in Carbon-Supported Palladium Catalysts. *Nat. Commun.* **2017**, *8* (1), 340. DOI: 10.1038/s41467-017-00421-x.

(27) Perathoner, S.; Ampelli, C.; Chen, S.; Passalacqua, R.; Su, D.; Centi, G. Photoactive Materials Based on Semiconducting Nanocarbons – a Challenge Opening New Possibilities for Photocatalysis. *J. Energy Chem.* **2017**, *26* (2), 207-218. DOI: 10.1016/j.jechem.2017.01.005.

(28) Tessonnier, J.-P.; Rosenthal, D.; Hansen, T. W.; Hess, C.; Schuster, M. E.; Blume, R.; Girgsdies, F.; Pfänder, N.; Timpe, O.; Su, D. S.; et al. Analysis of the Structure and Chemical Properties of Some Commercial Carbon Nanostructures. *Carbon* **2009**, *47* (7), 1779-1798. DOI: 10.1016/j.carbon.2009.02.032.

(29) Tessonnier, J.-P.; Ersen, O.; Weinberg, G.; Pham-Huu, C.; Su, D. S.; Schlögl, R. Selective Deposition of Metal Nanoparticles inside or Outside Multiwalled Carbon Nanotubes. *ACS Nano* **2009**, *3* (8), 2081-2089. DOI: 10.1021/nn900647q.

(30) Bluhm, H.; Hävecker, M.; Knop-Gericke, A.; Kiskinova, M.; Schlögl, R.; Salmeron, M. In Situ X-Ray Photoelectron Spectroscopy Studies of Gas-Solid Interfaces at near-Ambient Conditions. *MRS Bull.* **2007**, *32* (12), 1022-1030. DOI: 10.1557/mrs2007.211.

(31) Seah, M. Data Compilations: Their Use to Improve Measurement Certainty in Surface Analysis by AES and XPS. *Surf. Interface Anal.* **1986**, *9* (2), 85-98. DOI: 10.1002/sia.740090203.

(32) Shirley, D. A. High-Resolution X-Ray Photoemission Spectrum of the Valence Bands of Gold. *Phys. Rev, B.* **1972**, *5* (12), 4709. DOI: 10.1103/PhysRevB.5.4709.

(33) Doniach, S.; Sunjic, M. Many-Electron Singularity in X-Ray Photoemission and X-Ray Line Spectra from Metals. *J. Phys. C. Solid State Phys.* **1970**, *3* (2), 285. DOI: 10.1088/0022-3719/3/2/010.

(34) Kresse, G.; Hafner, J. Ab Initio Molecular Dynamics for Liquid Metals. *Phys. Rev, B.* **1993**, *47* (1), 558. DOI: 10.1016/0022-3093(95)00355-X.

(35) Blöchl, P. E. Projector Augmented-Wave Method. *Phys. Rev, B.* **1994**, *50* (24), 17953. DOI: 10.1103/PhysRevB.50.17953.

(36) Perdew, J. P.; Burke, K.; Ernzerhof, M. Generalized Gradient Approximation Made Simple. *Phys. Rev. Lett.* **1996**, *77* (18), 3865. DOI: 10.1103/PhysRevLett.77.3865.

(37) Hammer, B.; Hansen, L. B.; Nørskov, J. K. Improved Adsorption Energetics within Density-Functional Theory Using Revised Perdew-Burke-Ernzerhof Functionals. *Phys. Rev, B.* **1999**, *59* (11), 7413. DOI: 10.1103/PhysRevB.59.7413.

(38) Lu, W.; Wang, C.; Schmidt, M.; Bytautas, L.; Ho, K.; Ruedenberg, K. Molecule Intrinsic Minimal Basis Sets. I. Exact Resolution of Ab Initio Optimized Molecular Orbitals in Terms of Deformed Atomic Minimal-Basis Orbitals. *J. Chem. Phys.* **2004**, *120* (6), 2629-2637. DOI: 10.1063/1.1638731.

(39) Löwdin, P. O. On the Non-Orthogonality Problem Connected with the Use of Atomic Wave Functions in the Theory of Molecules and Crystals. *J. Chem. Phys.* **1950**, *18* (3), 365-375. DOI: 10.1063/1.1747632.

(40) Tessonnier, J.-P.; Rosenthal, D.; Girgsdies, F.; Amadou, J.; Begin, D.; Pham-Huu, C.; Su, D. S.; Schlögl, R. Influence of the Graphitisation of Hollow Carbon Nanofibers on Their Functionalisation and Subsequent Filling with Metal Nanoparticles. *Chem. Commun.* **2009**, (46), 7158-7160. DOI: 10.1039/b916150c.

(41) Shao, L.; Zhang, B.; Zhang, W.; Hong, S. Y.; Schlögl, R.; Su, D. S. The Role of Palladium Dynamics in the Surface Catalysis of Coupling Reactions. *Angew. Chem. Int. Ed.* **2013**, *52* (7), 2114-2117. DOI: 10.1002/anie.201207362.

(42) Yuvaraj, S.; Fan-Yuan, L.; Tsong-Huei, C.; Chuin-Tih, Y. Thermal Decomposition of Metal Nitrates in Air and Hydrogen Environments. *J. Phys. Chem. B* **2003**, *107* (4), 1044-1047. DOI: 10.1021/jp026961c.

(43) Tengco, J. M. M.; Lugo-José, Y. K.; Monnier, J. R.; Regalbuto, J. R. Chemisorption–XRD Particle Size Discrepancy of Carbon Supported Palladium: Carbon Decoration of Pd? *Catal. Today* **2015**, *246*, 9-14. DOI: 10.1016/j.cattod.2014.07.006.

(44) Rameshan, C.; Stadlmayr, W.; Penner, S.; Lorenz, H.; Mayr, L.; Hävecker, M.; Blume, R.; Rocha, T.; Teschner, D.; Knop-Gericke, A.; et al. In Situ XPS Study of Methanol Reforming on PdGa near-Surface Intermetallic Phases. *J. Catal.* **2012**, *290*, 126-137. DOI: 10.1016/j.jcat.2012.03.009.

(45) Teschner, D.; Pestryakov, A.; Kleimenov, E.; Hävecker, M.; Bluhm, H.; Sauer, H.; Knop-Gericke, A.; Schlögl, R. High-Pressure X-Ray Photoelectron Spectroscopy of Palladium Model Hydrogenation Catalysts.: Part 1: Effect of Gas Ambient and Temperature. *J. Catal.* **2005**, *230* (1), 186-194. DOI: 10.1016/j.jcat.2004.11.036.

(46) Zhao, Z.; Huang, X.; Li, M.; Wang, G.; Lee, C.; Zhu, E.; Duan, X.; Huang, Y. Synthesis of Stable Shape-Controlled Catalytically Active B-Palladium Hydride. *J. Am. Chem. Soc.* **2015**, *137* (50), 15672-15675. DOI: 10.1021/jacs.5b11543.

(47) Sinha, S.; Badrinarayanan, S.; Sinha, A. The Pd-H System Revisited: An XPS and UPS Study. *J. Phys. F. Met. Phys.* **1986**, *16* (9), L229. DOI: 10.1088/0305-4608/16/9/005.

(48) Contreras, R. C.; Guicheret, B.; Machado, B. F.; Rivera-Cárcamo, C.; Curiel Alvarez, M. A.; Valdez Salas, B.; Ruttert, M.; Placke, T.; Favre Réguillon, A.; Vanoye, L.; et al. Effect of Mesoporous Carbon Support Nature and Pretreatments on Palladium Loading, Dispersion and Apparent Catalytic Activity in Hydrogenation of Myrcene. *J. Catal.* **2019**, *372*, 226-244. DOI: https://doi.org/10.1016/j.jcat.2019.02.034.

(49) Wu, B.; Huang, H.; Yang, J.; Zheng, N.; Fu, G. Selective Hydrogenation of α,β-Unsaturated Aldehydes Catalyzed by Amine-Capped Platinum-Cobalt Nanocrystals. *Angew. Chem.* **2012**, *124* (14), 3496-3499. DOI: 10.1002/anie.201108593.

(50) Vu, K. B.; Bukhryakov, K. V.; Anjum, D. H.; Rodionov, V. O. Surface-Bound Ligands Modulate Chemoselectivity and Activity of a Bimetallic Nanoparticle Catalyst. *ACS Catal.* **2015**, *5* (4), 2529-2533. DOI: 10.1021/acscatal.5b00262.

(51) Durndell, L. J.; Parlett, C. M. A.; Hondow, N. S.; Isaacs, M. A.; Wilson, K.; Lee, A. F. Selectivity Control in Pt-Catalyzed Cinnamaldehyde Hydrogenation. *Sci. Rep.* **2015**, *5*, 9425, Article. DOI: 10.1038/srep09425.

(52) Murata, K.; Ogura, K.; Ohyama, J.; Sawabe, K.; Yamamoto, Y.; Arai, S.; Satsuma, A. Selective Hydrogenation of Cinnamaldehyde over the Stepped and Plane Surface of Pd Nanoparticles with Controlled Morphologies by CO Chemisorption. *ACS Appl. Mater. Interfaces.* **2020**, *12* (23), 26002-26012. DOI: 10.1021/acsami.0c05938.

(53) Cargnello, M.; Doan-Nguyen, V. V. T.; Gordon, T. R.; Diaz, R. E.; Stach, E. A.; Gorte, R. J.; Fornasiero, P.; Murray, C. B. Control of Metal Nanocrystal Size Reveals Metal-Support Interface Role for Ceria Catalysts. *Science* **2013**, *341* (6147), 771-773. DOI: doi:10.1126/science.1240148.

(54) Den Breejen, J.; Radstake, P.; Bezemer, G.; Bitter, J.; Frøseth, V.; Holmen, A.; Jong, K. d. On the Origin of the Cobalt Particle Size Effects in Fischer− Tropsch Catalysis. *J. Am. Chem. Soc.* **2009**, *131* (20), 7197-7203. DOI: 10.1021/ja901006x.

(55) Carballo, J. M. G.; Yang, J.; Holmen, A.; García-Rodríguez, S.; Rojas, S.; Ojeda, M.; Fierro, J. L. G. Catalytic Effects of Ruthenium Particle Size on the Fischer–Tropsch Synthesis. *J. Catal.* **2011**, *284* (1), 102-108. DOI: 10.1016/j.jcat.2011.09.008.

(56) Hibbitts, D.; Iglesia, E. Prevalence of Bimolecular Routes in the Activation of Diatomic Molecules with Strong Chemical Bonds (O_2, No, Co, N_2) on Catalytic Surfaces. *Acc. Chem. Res.* **2015**, *48* (5), 1254-1262. DOI: 10.1021/acs.accounts.5b00063.

(57) Allian, A. D.; Takanabe, K.; Fujdala, K. L.; Hao, X.; Truex, T. J.; Cai, J.; Buda, C.; Neurock, M.; Iglesia, E. Chemisorption of CO and Mechanism of CO Oxidation on Supported Platinum Nanoclusters. *J. Am. Chem. Soc.* **2011**, *133* (12), 4498-4517. DOI: 10.1021/ja110073u.

(58) Green, I. X.; Tang, W.; Neurock, M.; Yates, J. T. Spectroscopic Observation of Dual Catalytic Sites During Oxidation of CO on a Au/TiO_2 Catalyst. *Science* **2011**, *333* (6043), 736-739. DOI: 10.1126/science.1207272.

(59) Graciani, J.; Mudiyanselage, K.; Xu, F.; Baber, A. E.; Evans, J.; Senanayake, S. D.; Stacchiola, D. J.; Liu, P.; Hrbek, J.; Sanz, J. F. Highly Active Copper-Ceria and Copper-Ceria-Titania Catalysts for Methanol Synthesis from CO_2. *Science* **2014**, *345* (6196), 546-550. DOI: 10.1126/science.1253057.

(60) Rodriguez, J. A.; Liu, P.; Stacchiola, D. J.; Senanayake, S. D.; White, M. G.; Chen, J. G. Hydrogenation of CO_2 to Methanol: Importance of Metal–Oxide and Metal–Carbide Interfaces in the Activation of CO_2. *ACS Catal.* **2015**, *5* (11), 6696-6706. DOI: 10.1021/acscatal.5b01755.

(61) Nørskov, J. K.; Bligaard, T.; Logadottir, A.; Bahn, S.; Hansen, L. B.; Bollinger, M.; Bengaard, H.; Hammer, B.; Sljivancanin, Z.; Mavrikakis, M. Universality in Heterogeneous Catalysis. *J. Catal.* **2002**, *209* (2), 275-278. DOI: 10.1006/jcat.2002.3615.

(62) Yang, S.; Zhou, P.; Chen, L.; Sun, Q.; Wang, P.; Ding, S.; Jiang, A.; Zhang, D. W. Direct Observation of the Work Function Evolution of Graphene-Two-Dimensional Metal Contacts. *J. Mater. Chem. C.* **2014**, *2* (38), 8042-8046, 10.1039/C4TC01613K. DOI: 10.1039/C4TC01613K.

(63) Sygellou, L.; Paterakis, G.; Galiotis, C.; Tasis, D. Work Function Tuning of Reduced Graphene Oxide Thin Films. *J. Phys. Chem. C* **2016**, *120* (1), 281-290. DOI: 10.1021/acs.jpcc.5b09234.

(64) Ghogia, A. C.; Machado, B. F.; Cayez, S.; Nzihou, A.; Serp, P.; Soulantica, K.; Pham Minh, D. Beyond Confinement Effects in Fischer-Tropsch Co/Cnt Catalysts. *J. Catal.* **2021**, *397*, 156-171. DOI: 10.1016/j.jcat.2021.03.027.